12

Applications of Discrete Wavelet Transform in Optical Fibre Sensing

Allan C. L. Wong and Gang-Ding Peng
School of Electrical Engineering and Telecommunications
University of New South Wales
Australia

1. Introduction

This chapter presents a comprehensive review of recent advances in the applications of discrete wavelet transform (DWT) in optical fibre sensing. DWT, like Fourier transform (FT), is a versatile and powerful mathematical tool to process, extract and analyse data. In fibre sensing, DWT is particularly useful in the demodulation, demultiplexing and denoising of sensor data, as well as in the detection, extraction and interpretation of measurand-induced change from an acquired sensor signal.

Both continuous and discrete has found a wide variety of applications in fibre sensing, and has been extensively used for fibre Bragg gratings (FBGs) and interferometric sensors. For example, Chan et al. (2007, 2010) used wavelet transform (both continuous and discrete) in reducing noise and increasing wavelength detection accuracy of FBGs; Jones (2000a, 2000b) used in the edge detection and crack detection of FBGs embedded in some structures; Staszewski et al. (1997) and Bang & Kim (2010) used for the detection of acoustic wave induced by impact and defect in composite plates; Gangopadhyay et al. (2005, 2006) used to extract and analyse fibre Fabry-Perot interferometer signals; Lamela-Rivera et al. (2003) used in the detection of partial discharges from high-power transformers; Tomic et al. (2010) in pressure sensing; and Wang et al. (2001) in the health monitoring of ship hull structure.

This chapter begins with a brief introduction on the applications of DWT in fibre sensing. This follows by the principles and approaches of using DWT. Several important and fundamental formulations and concepts, such as the use of DWT in signal demodulation, demultiplexing and noise reduction will be presented. Next, four exemplary application cases of using DWT in fibre sensing are presented. More specifically, representative topics with regard to sensor signal analysis, signal demodulation, noise reduction and demultiplexing of multiplexed sensor systems are described in details. Finally, conclusions to summarise the chapter is given.

2. Principles and approaches

In fibre sensing, there are two areas of signal analysis that DWT has been widely employed, namely sensor signal demodulation and noise reduction. The former is accomplished by the theory of Multiresolution analysis (MRA) and the latter by the wavelet denoising. This section will describe these two DWT techniques qualitatively, and all of the subsequent examples are essentially based on them.

2.1 Sensor signal demodulation

The DWT demodulation technique presented here is used to demodulate and demultiplex many types of multiplexed sensor signals, and it works best with periodic sinusoidal functions, which is often the case for most interferometric signals. Excellent references in the theory and properties of wavelets can be found in (Daubechies, 1992; Mallet, 1998; Sidney Burrus et al., 1998; Vetterli & Kovacevic, 1995). In this section, only the concepts and results that are essential to the understanding of this demodulation technique are included. The principle of operation is based on the theory of MRA, a representation of DWT from a digital signal processing perspective (Mallet, 1989). In the MRA, the sensor signal can be represented as a wavelet series,

$$I(\lambda) = \sum_m c_J(m)\phi_{J,m}(\lambda) + \sum_m \sum_{j=1}^{J} d_j(m)\psi_{j,m}(\lambda) \,, \tag{2.1}$$

where $j, m \in Z$, and the integer J sets the highest decomposition level.

$$c_j(m) = \left\langle I(\lambda), \phi_{j,m}(\lambda) \right\rangle = \int I(\lambda)\varphi^*_{j,m}(\lambda)d\lambda \tag{2.2}$$

are the jth-level DWT approximation coefficients, and

$$d_j(m) = \left\langle I(\lambda), \psi_{j,m}(\lambda) \right\rangle = \int I(\lambda)\psi^*_{j,m}(\lambda)d\lambda \tag{2.3}$$

are the jth-level DWT detail coefficients. * denotes the operation of complex conjugation. $\phi_{j,m}(\lambda) = 2^{j/2}\phi(2^j\lambda - m)$ is the scaling function, and $\psi_{j,m}(\lambda) = 2^{j/2}\psi(2^j\lambda - m)$ is the wavelet function. The DWT coefficients can be computed by a multistage two-channel quadrature mirror filter bank (QMFB). This is formed by the scaling function acting as a low-pass filter, i.e., $\phi(\lambda) = \sum_m h(m)\sqrt{2}\phi(2\lambda - m)$, where $h(m)$, $m \in Z$, are the low-pass filter coefficients. The complementary wavelet function acts as a high-pass filter, i.e., $\psi(\lambda) = \sum_m g(m)\sqrt{2}\phi(2\lambda - m)$, where $g(m)$ are the high-pass filter coefficients. The filter coefficients are related by $g(m) = (-1)^m h(1-m)$. In other words, in the QMFB the scaling and wavelet functions simultaneously perform the low-pass and high-pass filtering on the sensor signal. At the jth-stage of the QMFB, the DWT approximation coefficients are given by,

$$A_j = c_j(m) = \sum_k h(k-2m)c_{j-1}(k) \,, \tag{2.4}$$

and the DWT detail coefficients are given by,

$$D_j = d_j(m) = \sum_k g(k-2m)c_{j-1}(k) \,. \tag{2.5}$$

Then, Eq. (2.1) can be expressed in the form,

$$I(\lambda) = \sum_m A_J + \sum_m \sum_{j=1}^{J} D_j \,. \tag{2.6}$$

From this representation, the jth-level DWT coefficients can be computed by convolving the QMFB with the $(j-1)$th-level approximation coefficients, i.e., $A_{j-1} = A_j + D_j$. The schematic

diagram of the multistage decomposition operation using the QMFB is shown in Fig. 2.1. By repeating this decomposition in cascade using the most recent A_j as inputs, we can compute the DWT coefficients to the resolution level of interest. The usefulness of the MRA representation is that a signal can be decomposed into different levels of wavelet coefficients according to the frequency components that comprised the whole signal. The higher the wavelet levels, the lower the frequency components of the signal remain. Fig. 2.2 shows graphically the frequency representation of a signal being decomposed into various wavelet levels. f_c is the centre frequency of the whole spectral bandwidth of the signal. If the multiplexed sensor signal is tailored in such a way that each sensor has a different (signal) frequency, after this cascaded operation, their original sensor signals will appear on different wavelet levels.

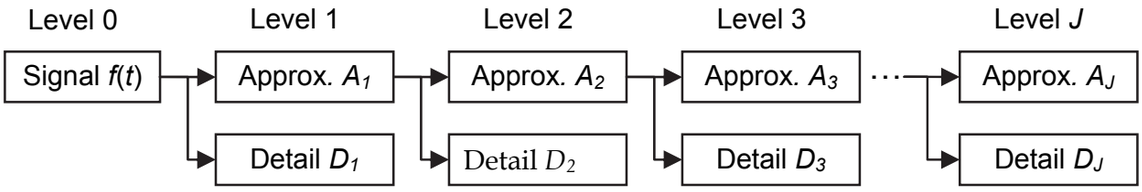

Fig. 2.1. Multistage decomposition of a signal using QMFB.

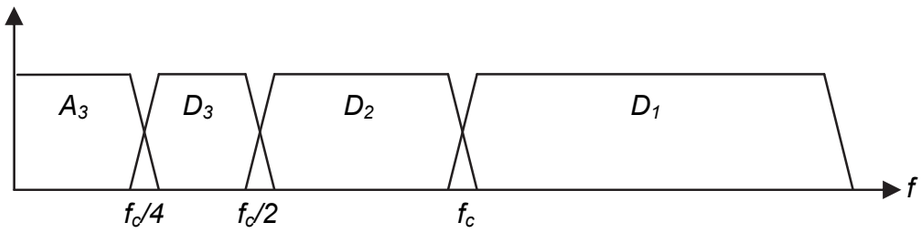

Fig. 2.2. Frequency representation of a signal decomposed into various wavelet levels.

2.2 Wavelet denoising

Wavelet denoising (Donoho, 1994) is a nonlinear noise reduction technique based on the DWT to remove/reduce the noise in the signal while preserving the overall signal features. The generic denoising algorithm is depicted in Fig. 2.3. In principle, wavelet denoising attempts to decompose a signal using the DWT to obtain the wavelet coefficients, and then apply a thresholding method or a shrinkage rule to each wavelet coefficient. The threshold can be obtained by using some risk estimators or by empirically finding a value. The method then either keeps or shrinks all wavelet coefficients that are above the threshold, and suppresses all those below the threshold. Then, the signal is reconstructed by taking the inverse DWT with the noisy part being removed. Here, two denoising techniques that are frequently employed in fibre sensing are discussed, namely hard thresholding (HT) and block-level thresholding (BLT). The former is a simple and effective method, while the latter is automatically incorporated with the DWT demodulation technique, making it a very attractive and convenient denoising method.

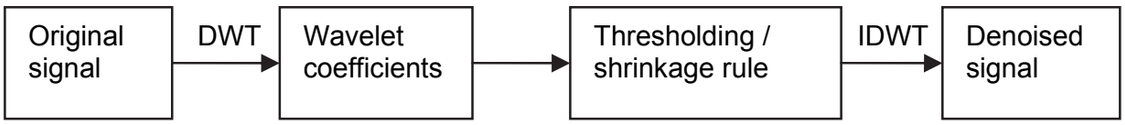

Fig. 2.3. Generic wavelet denoising algorithm.

2.2.1 Hard thresholding

When a sensor signal is acquired from a measurement system, the signal consists of broadband noise caused by the quality of the sensor, as well as the quantisation and finite resolution errors of the equipment. It is known that broadband noise is difficult to remove using conventional filtering without altering the signal. But this can be done by the HT wavelet denoising. Let the sensor signal intensity be represented as a wavelet series,

$$I(\lambda) = \sum_{m,n=-\infty}^{\infty} \alpha_{m,n} \psi_{m,n}(\lambda) , \tag{2.7}$$

where $\psi_{m,n}(\lambda) = 2^{m/2} \psi(2^m \lambda - n)$, $\psi \in L^2(\Re)$, $m, n \in Z$ are the orthonormal wavelet basis functions. By taking the DWT, the wavelet coefficients are,

$$\alpha_{m,n} = \left\langle \psi_{m,n}(\lambda), I(\lambda) \right\rangle = \int_{-\infty}^{\infty} \psi^*_{m,n}(\lambda) I(\lambda) d\lambda . \tag{2.8}$$

The HT then sets a threshold value, h, to the wavelet coefficients, such that any coefficients below the threshold are suppressed, whereas the coefficients above the threshold are retained. Since the noise components are usually of low magnitude, the threshold can be set to a value high enough to eliminate the noisy coefficients, and low enough to retain useful signal coefficients. The HT operation can be represented by (Wong et al., 2005),

$$\xi_h(\alpha_{m,n}) = \hat{\alpha}_{m,n} = \begin{cases} \alpha_{m,n}, & |\alpha_{m,n}| > h \\ 0, & |\alpha_{m,n}| \le h \end{cases} . \tag{2.9}$$

Since the HT is applied to the entire spectral range of the sensor signal, the broadband noise can be effectively removed. Once the noisy coefficients are removed, the signal can be reconstructed by taking the inverse DWT,

$$I'(\lambda) = \sum_{m,n=-\infty}^{\infty} \hat{\alpha}_{m,n} \psi_{m,n}(\lambda) . \tag{2.10}$$

From another perspective, suppose a sensor signal consists of an ideal noise-free part $f(\lambda)$ and a noisy part $\sigma(\lambda)$ with noise level p, i.e., $I(\lambda) = f(\lambda) + p\sigma(\lambda)$. If we set $h = p$, i.e., setting the threshold equal to the noise level, then the HT will suppress the noisy coefficients to zero while retaining the noise-free coefficients unaffected. The ideal case is to have $|I(\lambda) - f(\lambda)| \to 0$, i.e., the reconstructed signal is as close as practicable to the ideal, noise-free signal.

2.2.2 Block-level thresholding

The BLT can be considered as a modified version of the block-thresholding method (Wong et al., 2006b). In the block-thresholding method, instead of applying a threshold to each wavelet coefficient term-by-term (as is for HT), the threshold is applied to a block of wavelet coefficients, with the threshold value determined by calculating and minimising the risk using the block James-Stein estimator. On the other hand, the BLT method attempts to set an entire level of wavelet coefficients as a block, such that the entire level is either retained or discarded. There is no need to estimate the risk or to find a value empirically in order to obtain the threshold value. For example, if the sensor signal has Gaussian white noise associated with it, such that the noise components spanned the whole frequency range of the signal. From the theory of MRA, the 1st-level detail coefficients account for the upper-half of the whole frequency range of the original signal, the 2nd-level account for the upper-half frequency range of the 1st-level approximation coefficients, and so on (c.f. Fig. 2.2). Therefore, the first two levels of detail coefficients cover 75 % of the whole frequency range of the sensor signal, and the noise components within this range will be removed if we discard the detail coefficients at these levels. For the signal expressed in the form of Eq. (2.6) with levels $j = 1,2,...,J$, the BLT operation for a chosen level of approximation coefficients ($j = J_A$) used to demodulate the sensor signal is given by,

$$BLT(j = J_A) \Rightarrow I(\lambda) = \begin{cases} \sum_m A_{J_A}, & \text{for } j = J_A \\ 0, & \text{otherwise} \end{cases}, \tag{2.11}$$

Similarly, for a chosen level of detail coefficients ($j = J_D$) used to demodulate the sensor signal, the BLT operation is given by,

$$BLT(j = J_D) \Rightarrow I(\lambda) = \begin{cases} \sum_m D_{J_D}, & \text{for } j = J_D \\ 0, & \text{otherwise} \end{cases}. \tag{2.12}$$

In other words, the BLT discards all the levels of detail coefficients that are at (for approximation coefficients) or below (for detail coefficients) the desired level chosen to be used for sensor signal demodulation. Additionally, the BLT denoising technique can be applied as a standalone technique for any type of signal. In a more general form, the BLT for a chosen level j_{BLT}, where $1 \le j_{BLT} \le J$, is given by (Wong et al., 2007a),

$$BLT(j_{BLT}) \Rightarrow I(\lambda) = \begin{cases} \sum_m A_J + \sum_m \sum_{j=j_{BLT}+1}^{J} D_j, & \text{for } j_{BLT} < j \le J \\ \sum_m A_J, & \text{for } j = j_{BLT} \\ 0, & \text{for } 1 \le j < j_{BLT} \end{cases}. \tag{2.13}$$

An inverse DWT is then applied to the wavelet coefficients to reconstruct the signal with the noisy part removed. The choice of j_{BLT} requires the signal to preserve its characteristic features for demodulation purposes, while being able to maximally remove the broadband noise components associated with it.

In the subsequent sections, four exemplary applications, which are the research works conducted by the authors, will be presented to demonstrate the power and versatility of the DWT.

3. Application case 1 – simultaneous multi-sensor signal demodulation

In the first example, a new simultaneous demodulation technique was proposed for a multiplexed fibre Fizeau interferometer (FFI) and FBG sensor system, based on the DWT technique described in the last section (Wong et al., 2006a, 2006b). In relation to this demodulation technique, the BLT denoising technique was applied automatically and simultaneously to reduce the noise associated with the sensor signal. It is known that FFIs and FBGs are two of the most widely studied types of fibre-optic sensors (Lee, 2003). They have distinct measurand-induced responses and dynamic ranges, and hence, when they are combined together, they can measure different measurands simultaneously. This demodulation technique outperforms currently reported techniques, and the key advantages are: (i) it overcomes the disadvantages associated with interferometric methods; (ii) it only requires a simple setup to interrogate and multiplex the sensors. All the data acquisition, signal processing, and calculations are carried out digitally by a computer program, and no complicated demodulating electronics are needed; (iii) it is a completely passive system that does not require any mechanical moving parts or active modulation, making it especially suited for continuous long-term quasi-static sensing; (iv) and it automatically reduces the signal noise through the BLT, without the need of any additional filtering techniques.

The FFI and FBG sensors are multiplexed using a hybrid of spatial-frequency-division multiplexing (SFDM) and wavelength-division multiplexing (WDM). Specifically, SFDM is used to multiplex the FFI sensors, in that each sensor produces a sinusoidal interference pattern with the spatial frequency specified by the cavity length. The multiplexed FFIs signal can then be demodulated using the FT peak detection method, which will be described later. For FBG sensors, WDM is employed in order to take the advantage of the wavelength-encoded nature. In the wavelength domain, each FBG has a narrowband Bragg peak in the reflection spectrum. As a result, the multiplexed signal is of two extremes: the FBG signal (i.e., the main peak) is localised with compact support in the original (wavelength) domain, but spans across the entire spectral bandwidth in the dual (spatial-frequency domain). The opposite case applies to the FFI signal. That is, in the original domain the signal is spanned along the spectral bandwidth of the light source. But in the dual domain, the signal is localised with compact support, and is shown as a sharp peak. In this case, the multiplexed signal can be easily separated by the DWT technique and individual sensor signals will appear on two distinct wavelet levels.

Fig. 3.1 (a) shows the experimental setup for the sensor system, An amplified spontaneous emission (ASE) light source was connected to a 3-dB fibre coupler to illuminate the FFI and FBG sensors that are serially multiplexed. This reflected signal was acquired by an optical spectrum analyser (OSA) and transferred to a computer. The multiplexed signal is the superposition of the two individual sensor signals. Assuming no insertion loss, for N FFIs and M FBGs, the measured spectrum is of the form (Wong et al., 2006b):

$$\begin{aligned} I(\lambda) &= A(\lambda)\left(\sum I(\lambda)_{FFI} + \sum I(\lambda)_{FBG}\right) \\ &= A(\lambda)\left\{\sum_{k=1}^{N} r_{1,k} r_{2,k}\left[1 + V_k S(\lambda)\cos(4\pi d_k / \lambda)\right] + \sum_{l=1}^{M} R_{B,l}\exp\left[-(\lambda - \lambda_{B,l})^2 / 2\delta\lambda_{B,l}^2\right]\right\}, \end{aligned} \tag{3.1}$$

where $A(\lambda)$ is the incident light source intensity, r_i are the reflection coefficients of the two fibre ends that form the FFI cavity, d is the cavity length, V is the fringe visibility, $S(\lambda)$ is the erbium-doped fibre (EDF) amplifier spectral profile, λ_B is the centre Bragg wavelength, R_B is the peak reflectivity of the FBG, and $\delta\lambda_B$ is a parameter related to the FBG bandwidth. A typical multiplexed signal for $N = M = 1$ is shown in Fig. 3.1 (b). From the figure, the FBG can be identified by the distinct narrowband peak (around 1533 nm), whereas the FFI produced a sinusoidal interference pattern that spanned the light source bandwidth, and superimposed on its spectral profile.

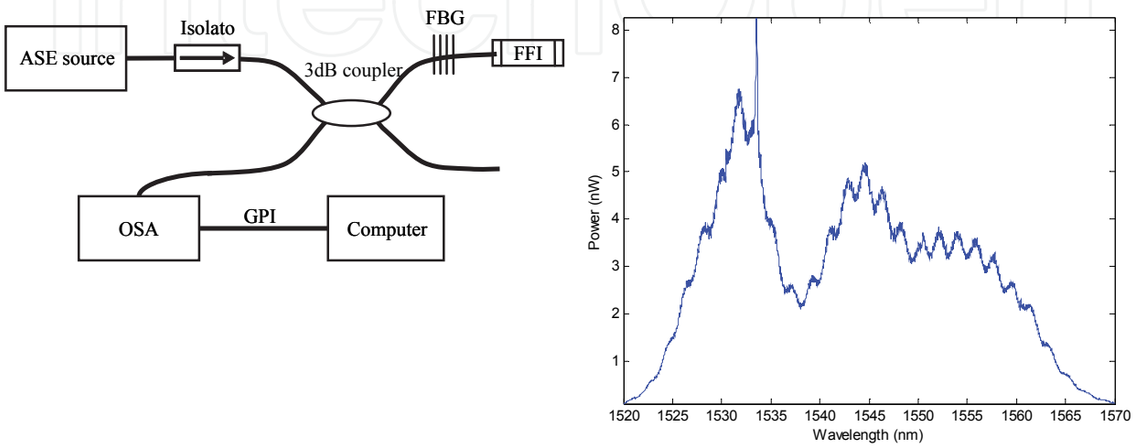

(a) (b)

Fig. 3.1. (a) Experimental setup for the multiplexed FFI and FBG sensor system; and (b) a typical multiplexed sensor signal.

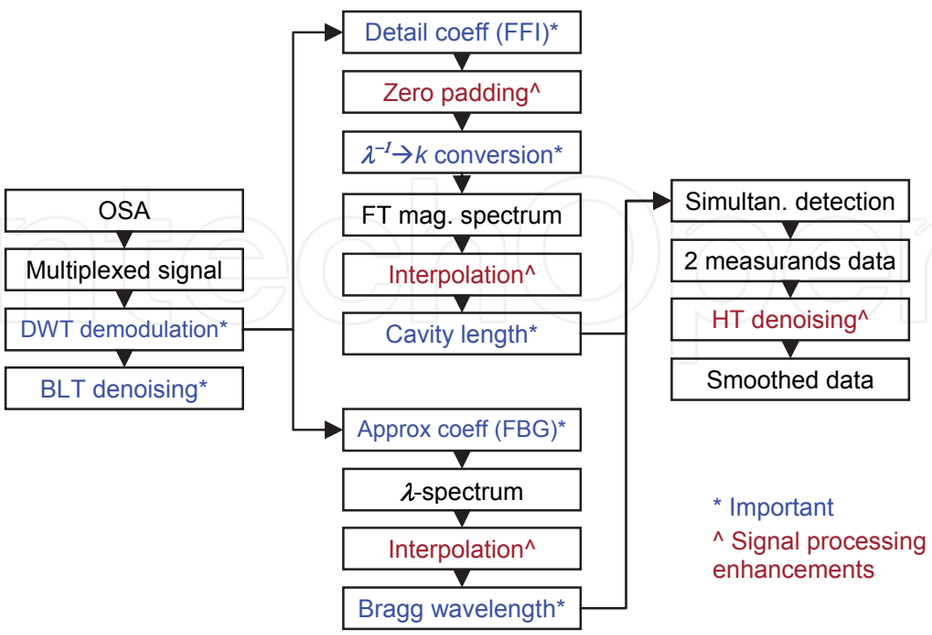

Fig. 3.2. Simultaneous demodulation algorithm with wavelet denoising.

The simultaneous demodulation algorithm is depicted in Fig. 3.2. For a multiplexed signal retrieved from the OSA, the DWT was applied to decompose it into multilevel wavelet coefficients. In parallel to the demodulation, the BLT was applied simultaneously such that the decomposed signal was denoised. The discrete Meyer wavelet was chosen to be the kernel function for DWT because the number of vanishing moments and regularity are suitable for analysing this type of multiplexed signal. For the FBG sensor, since the received signal from the OSA was a function of wavelength, the Bragg wavelength can be determined directly from a level of approximation coefficients, which effectively gave the denoised version of the original spectrum. The BLT technique automatically discarded the wavelet levels that were below the chosen level of approximation coefficients for the FBG signal, and thus reduced the signal noise without explicitly applying any additional filtering technique. Then, an interpolation utilising the piecewise-continuous cubic-spline function was applied to the Bragg peak to increase the wavelength resolution. Next, the cavity length of the FFI was determined. After taking the DWT, the detail coefficients were indeed the original interference pattern of the FFI, which was then demodulated using the FT peak detection method. First, the signal was Fourier transformed and each sensor had its own peak in the magnitude spectrum. The important step was to convert the variables of the detail coefficients from wavelength to wavenumber. In doing so, the FT dual-domain variable was related to the sensor cavity length. The cavity length can then be obtained directly from the location of the amplitude peak in the magnitude spectrum (Wong et al., 2005). Once the characteristic change of both sensors are known, i.e., Bragg wavelength of the FBG and cavity length of the FFI, simultaneous measurement of two measurands can be achieved by monitoring the changes of both sensors. In order to do so, the measurands-induced responses, i.e., the elements in the sensitivity matrix need to be determined. The HT denoising technique (described in previous section) can be used to denoise and smooth out the measured data. Thus, this demodulation technique provided a complete process for a practical sensor system from the acquisition of raw data to human understandable measurand outputs, and all steps were performed digitally by a computer program.

Having described in details the demodulation algorithm, for an acquired multiplexed signal [Fig. 3.1 (b)], after taking the DWT, the approximation coefficients that represent the FBG signal is shown in Fig. 3.3 (a). The approximation coefficients give a smoothed and noise-reduced version of the original noisy signal. Fig. 3.3 (b) shows the magnification around the Bragg peak, and the Bragg wavelength shift can be found directly by employing a wavelength detection method. A resolution of ~1.2 pm after interpolation was achieved. For the FFI sensor, after taking the DWT, Fig. 3.4 (a) shows the detail coefficients, which effectively represented the mean-removed and windowed version of the original interference pattern. Fig. 3.4 (b) shows the Fourier transformed magnitude spectrum of the detail coefficients around the amplitude peak. It can be seen that, after conversion of x-variable, the cavity length can be directly determined from its position in the magnitude spectrum. A resolution of ~0.04 μm was achieved after interpolation.

An application of this demodulation technique was demonstrated through the simultaneous measurement of strain and temperature of an aluminium (Al) plate. With the setup from Fig. 3.1 (a) the FBG was loosely adhered onto the Al-plate, such that it was not affected by the strain field. The FFI adhered firmly onto the Al-plate next to the FBG using some superglue, and so it was affected by both strain and temperature changes of the plate. Before proceeding to the actual experiment, the coefficients in the sensitivity matrix needed to be determined. To illustrate this, let the two sensors be represented as,

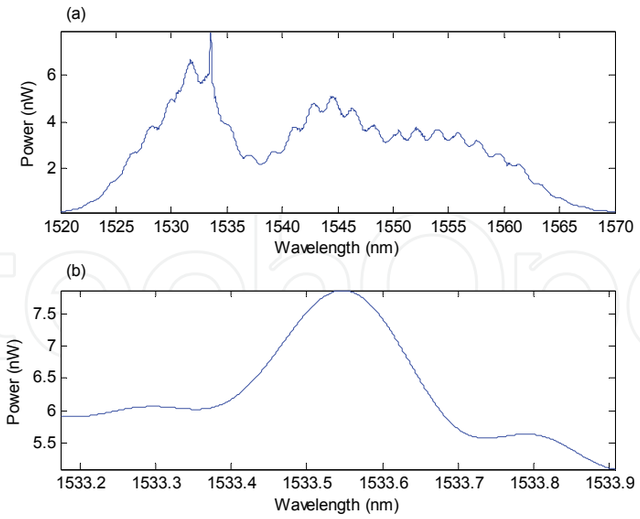

Fig. 3.3. (a) Approximation coefficients for the FBG; (b) around the Bragg peak.

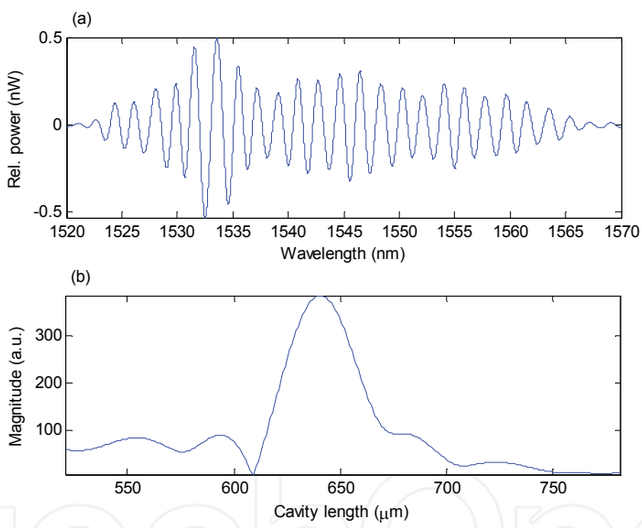

Fig. 3.4. (a) Detail coefficients for the FFI; (b) FT magnitude spectrum around the peak.

$$\begin{aligned} \Delta\zeta_1 &= K_{1\varepsilon}\Delta\varepsilon + K_{1T}\Delta T \\ \Delta\zeta_2 &= K_{2\varepsilon}\Delta\varepsilon + K_{2T}\Delta T \end{aligned}, \tag{3.2}$$

where $\Delta\zeta_i$ are the measurand-induced physical change of the sensors, and K_{ij} are the measurand-induced responses (i.e., sensitivity coefficients). $\Delta\varepsilon$ and ΔT are the strain and temperature changes, respectively. Eq. (3.2) is a set of two simultaneous linear equations, which can be expressed in matrix form as,

$$\begin{pmatrix} \Delta\zeta_1 \\ \Delta\zeta_2 \end{pmatrix} = \begin{pmatrix} K_{1\varepsilon} & K_{1T} \\ K_{2\varepsilon} & K_{2T} \end{pmatrix} \begin{pmatrix} \Delta\varepsilon \\ \Delta T \end{pmatrix}. \tag{3.3}$$

This equation can be solved for the measurand vector by inverting the *K*-matrix, i.e.,

$$\begin{pmatrix} \Delta\varepsilon \\ \Delta T \end{pmatrix} = \frac{1}{\det(K)} \begin{pmatrix} K_{2T} & -K_{1T} \\ -K_{2\varepsilon} & K_{1\varepsilon} \end{pmatrix} \begin{pmatrix} \Delta\zeta_1 \\ \Delta\zeta_2 \end{pmatrix}, \tag{3.4}$$

where $\det(K) = K_{1\varepsilon}K_{2T} - K_{1T}K_{2\varepsilon} \neq 0$. This shows the strain and temperature can be simultaneously separated and measured provided the elements in the square matrix are pre-determined. This can be done by measuring one measurand (while the other kept constant) at a time against the spectral response of each sensor. For this sensor arrangement, with the details described in (Wong et al., 2006b), the strain and temperature responses of the FBG and FFI sensors are shown in Figs. 3.5 and 3.6, respectively. From the linear regression fits, for the FBG sensor the strain and temperature sensitivity coefficients are 1.2 pm/με and 10.4 pm/°C, respectively; whereas for the FFI sensor, the respective sensitivity coefficients are 4.06×10^4 pm/με and 1.12×10^6 pm/°C. Since the FBG was not affected by strain change, the system of linear equations is given by,

$$\begin{pmatrix} \Delta d \\ \Delta\lambda_B \end{pmatrix} = \begin{pmatrix} 4.06\times10^4 & 1.12\times10^6 \\ 0 & 10.4 \end{pmatrix} \begin{pmatrix} \Delta\varepsilon \\ \Delta T \end{pmatrix}, \tag{3.5}$$

and

$$\begin{pmatrix} \Delta\varepsilon \\ \Delta T \end{pmatrix} = \begin{pmatrix} 2.5\times10^{-5} & -2.7 \\ 0 & 9.6\times10^{-2} \end{pmatrix} \begin{pmatrix} \Delta d \\ \Delta\lambda_B \end{pmatrix}, \tag{3.6}$$

where Δd and $\Delta\lambda_B$ are the FFI cavity length change and FBG Bragg wavelength shift, respectively. The sensors were left in the laboratory overnight for a period of 14 hours, with no external axial strain applied. A LabVIEW program was written to acquire the sensor signal in real-time at a rate of ~6 s per reading. The FFI subjected to both the thermal strain and temperature change of the Al-plate, while the FBG subjected to temperature change only. By using Eq. (3.6), the separated effects of thermal strain and temperature change over the measured period are shown in Fig. 3.7. Although both sensors experienced the same temperature change, the thermal strain of the Al-plate did not correlate very well with its temperature change. This is because the FBG was loosely adhered onto the Al-plate, it was influenced by the surrounding environment and temperature change more than the thermal response of the Al-plate.

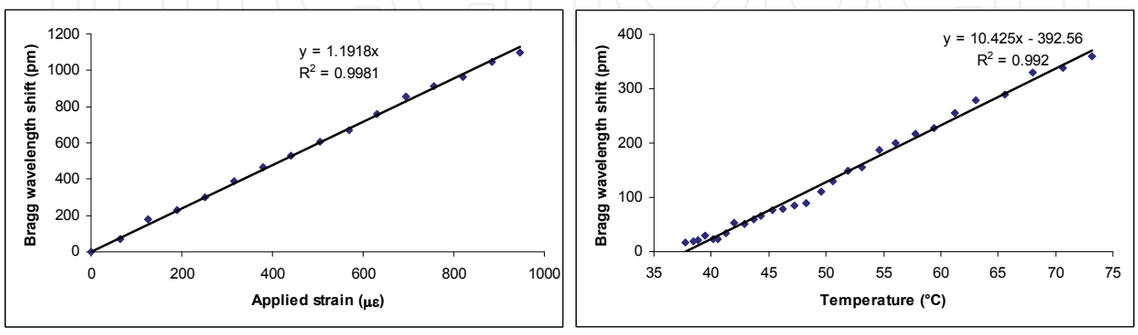

(a) (b)

Fig. 3.5. (a) Strain and (b) temperature responses of the FBG sensor.

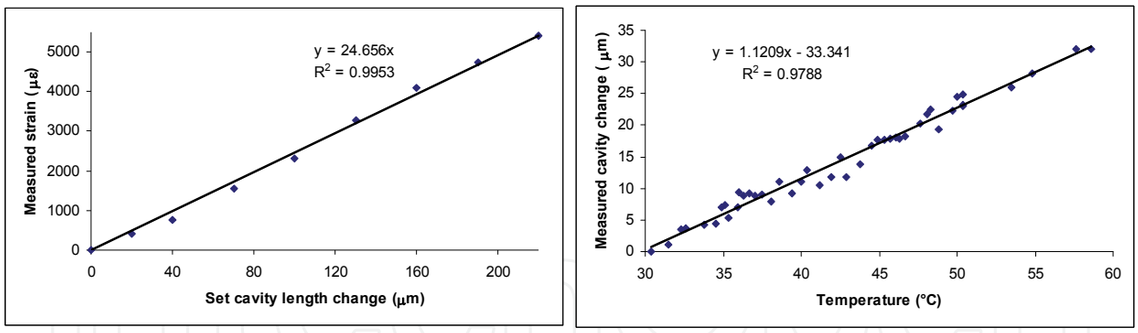

(a) (b)

Fig. 3.6. (a) Strain and (b) temperature responses of the FFI sensor.

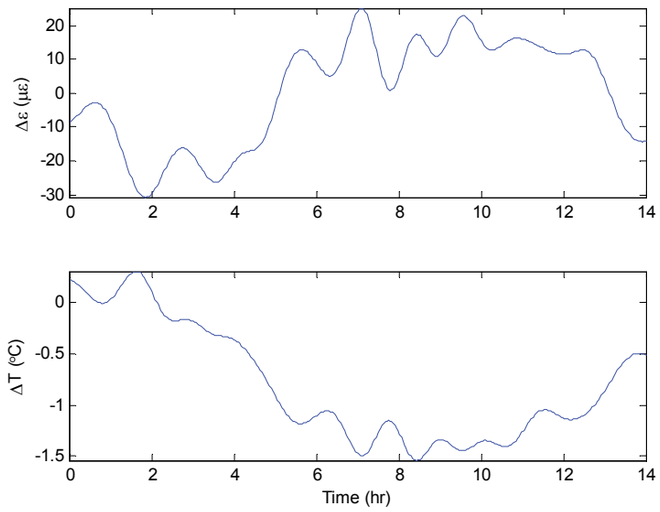

Fig. 3.7. Simultaneous measurement of strain and temperature of Al-plate.

4. Application case 2 – multiplexing and demultiplexing of multi-sensors

In the second example, a new type of FBG called amplitude-modulated chirped FBGs (AMCFBGs) was designed and fabricated, and based on that, a new multiplexing technique called spectral overlap multiplexing was proposed and experimentally demonstrated (Childs et al., 2010, Wong et al., 2007a, 2007b, 2010). We show that, the DWT played a central role in the demultiplexing, demodulation and analysis of these multiplexed novel sensor signals. The AMCFBGs are similar to ordinary chirped FBGs, i.e., they have a broad and flat reflection spectrum. The subtle difference is the addition of an amplitude-modulation function to the refractive index modulation of the fibre core, which is achieved by varying the induced DC refractive index during the writing process. With this index modulation, the reflection spectrum has a unique signature – a sinusoidal modulation on its flat-top region. The amplitude-modulation function for the refractive index modulation is given by $f_d(z) = w \cdot \sin^2\left(\pi dz / L_g\right)$, where w is an apodisation function such as a raised-cosine function, d is the number of periods (frequency) of modulation, and L_g is the length of the

grating. The reflection spectrum for one AMCFBG can be approximated by the expression (Wong et al., 2007a),

$$R(\lambda) \approx \chi_{\left(\lambda_{\min},\lambda_{\min}+c_L L_g\right)}(\lambda)\left[R_{\min}+\left(R_{\max}-R_{\min}\right) f_d\left(\frac{\lambda-\lambda_{\min}}{c_L}\right)\right], \tag{4.1}$$

where λ_{min} is the initial wavelength of the grating, R_{min} and R_{max} are the reflectivities of the troughs and peaks of the grating spectrum, respectively, c_L is the linear chirp rate of the phase mask used for writing the gratings, and $\chi_I(x)$ is the characteristic function on the interval I which equals 1 when x is an element of I and zero otherwise. The fabrication procedure can be found in (Wong et al., 2007b). As an example of an AMCFBG that we fabricated, Fig. 4.1 (a) shows the amplitude-modulation function with a raised-cosine apodisation, d = 5 and L_g = 10 mm; and Fig. 4.1 (b) shows the corresponding measured reflection spectrum.

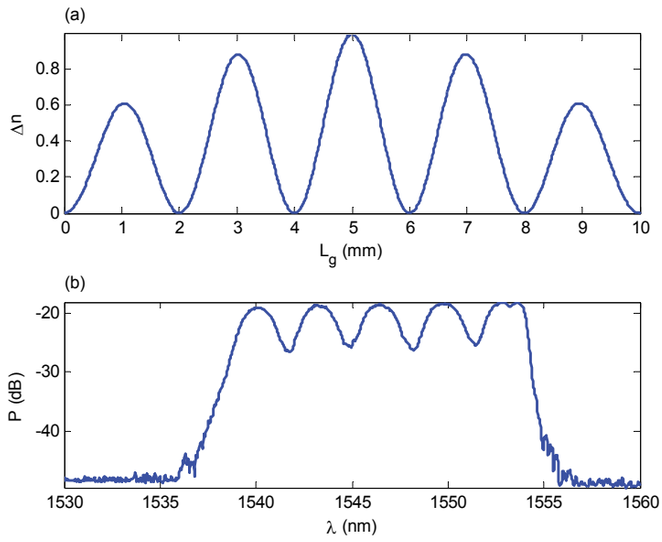

Fig. 4.1. (a) Index modulation function used in the fabrication; (b) measured reflection spectrum of the AMCFBG.

In the wavelength domain, ordinary FBGs cannot be easily distinguished if they are spectrally overlapped. Using the amplitude-modulation as a unique signature for each grating, the AMCFBGs are able to completely overlap one another having the same spectral characteristics, i.e., centre Bragg wavelength, bandwidth and reflectivity, yet still be uniquely distinguishable from each other. The uniqueness of each AMCFBG is defined by the number of periods (spatial-frequency) of its amplitude-modulation, and for a set of spectrally-overlapped gratings, no two gratings can have the same number of periods. With such unique signatures for the AMCFBGs, viable methods are needed to demultiplex and demodulate the multiplexed signals, and that was accomplished by using the DWT technique similar to that applied in the previous section. This is the basis of the new spectral overlap multiplexing technique. Since this multiplexing is fully compatible with the WDM, the sensor count can potentially be increased by several folds.

To demonstrate the spectral overlap multiplexing using AMCFBGs, we performed two experiments. In the first experiment, two spectrally overlapped gratings, S1 and S2, were employed, and the schematic diagram of the setup is depicted in Fig. 4.2. The individual spectra of S1 and S2, as well as the combined spectra are shown in Fig. 4.3 (a) – 4.3 (c), respectively. It is clear that, WDM scheme would not allow such overlapping, and without a suitable signal processing technique, it is unlikely the multiplexed signal be separated and analysed. However, by taking the DWT, the unique signatures, i.e., the

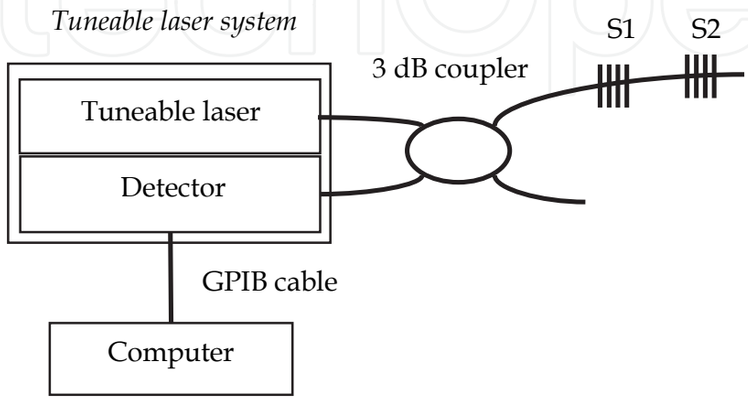

Fig. 4.2. Experimental setup of the multiplexed AMCFBG system.

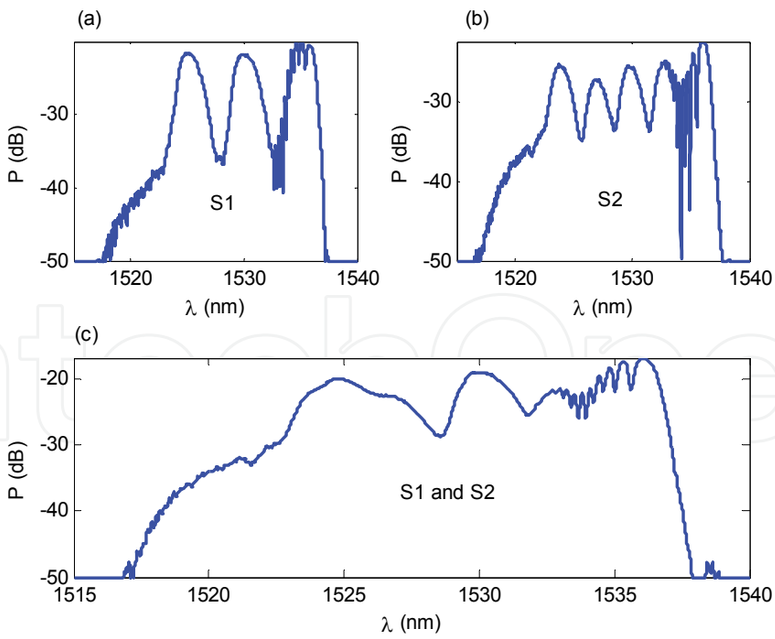

Fig. 4.3. Reflection spectrum of (a) S1, (b) S2, and (c) combined signal.

sinusoidal modulations of the gratings, can be recovered. Fig. 4.4 shows that the detail coefficients of the two gratings, and the unique modulated periods are unambiguously identified. That is, the multiplexed signal has been successfully demodulated whereby the

measurand-induced wavelength shifts can be measured individually by tracking the 'phase-shift' of the modulations. The strain response and crosstalk of the multiplexed AMCFBGs under this multiplexing scheme were conducted. A total of ten 20-cent coins (each weighs 11.3 g, which corresponds to a strain of 125 με) were applied to S1, while S2 was left unstrained. For each coin applied, ten readings were taken. Fig. 4.5 (a) shows the

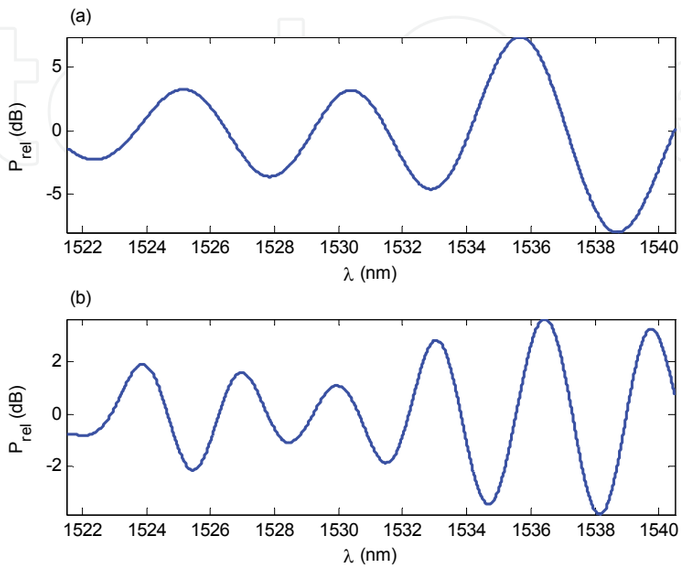

Fig. 4.4. Detail coefficients for (a) S1 and (b) S2 gratings.

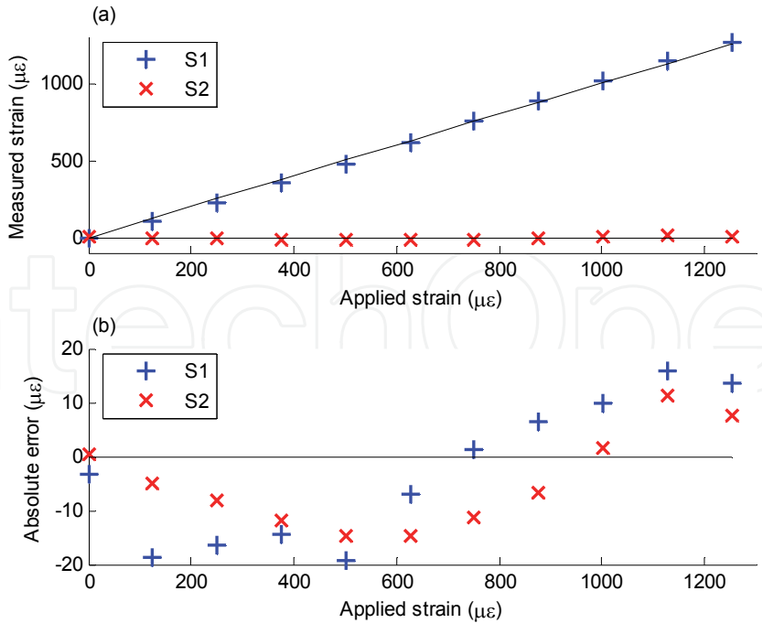

Fig. 4.5. (a) Strain measurements and (b) absolute errors of S1 (strained) and S2 (unstrained).

measured strain responses of S1 and S2 as a function of applied strain. The strain values were obtained by using the DWT technique mentioned before. The lines are the ideal

strain values. It can be seen that S1 measured the strain very accurately. For strains applied up to 1250 με, the absolute error is within ±20 με as shown in Fig. 4.5 (b). The corresponding strain response of S2 showed little crosstalk, with a maximum value of about 16 με as shown in Fig. 4.5 (b). This small amount of crosstalk implies that adverse effects, such as spectral shadowing, did not impose much of a problem on this multiplexing technique.

In the second experiment, simultaneous strain and temperature measurement of an Al-alloy plate was carried out. The experiment was similar to that in the previous section. That is, the AMCFBG sensors were first characterised to obtain the strain and temperature sensitivity coefficients, then simultaneous two-parameter measurement of the material was performed. Strain and temperature changes were obtained by measuring the wavelength (i.e., 'phase') shifts of the sensors and calculating their corresponding values. Two overlapped AMCFBGs were used, and to effectively utilise the advantage of having the same Bragg wavelength, the reference grating method (Wong et al., 2007b) was used. In such method, the strain sensor was firmly attached onto the structure, while the temperature sensor was placed under the same environmental conditions but unstrained. As such, the former experienced wavelength shifts due to both strain and temperature, while the latter only experienced the shift due to temperature change. With reference to Eq. (3.3), the set of simultaneous equations is given by,

$$\begin{pmatrix} \Delta\lambda_{B1}/\lambda_{B1} \\ \Delta\lambda_{B2}/\lambda_{B2} \end{pmatrix} = \begin{pmatrix} k_{1\varepsilon} & k_{1T} \\ 0 & k_{2T} \end{pmatrix} \begin{pmatrix} \Delta\varepsilon \\ \Delta T \end{pmatrix}, \text{ or } \begin{pmatrix} \Delta\varepsilon \\ \Delta T \end{pmatrix} = \frac{1}{k_{1\varepsilon}k_{2T}} \begin{pmatrix} k_{2T} & -k_{1T} \\ 0 & k_{1\varepsilon} \end{pmatrix} \begin{pmatrix} \Delta\lambda_{B1}/\lambda_{B1} \\ \Delta\lambda_{B2}/\lambda_{B2} \end{pmatrix}, \tag{4.2}$$

where the subscripts 1 and 2 represent strain and temperature sensors, respectively. Some approximations are made: (a) as both sensors experience the same temperature change, $k_T = k_{1T} = k_{2T}$; (b) the Bragg wavelengths are the same for both sensors and so $\lambda_B = \lambda_{B1} = \lambda_{B2}$. By setting $k_\varepsilon = k_{1\varepsilon}$ and modifying Eq. (4.2), the expressions for strain and temperature change are then given by,

$$\Delta\varepsilon = \frac{1}{k_\varepsilon}\frac{\left(\Delta\lambda_{B1} - \Delta\lambda_{B2}\right)}{\lambda_B}; \text{ and } \Delta T = \frac{1}{k_T}\frac{\Delta\lambda_{B2}}{\lambda_B}. \tag{4.3}$$

Eq. (4.3) shows that the strain of a structure under test can be simply obtained from the differential wavelength shift between the two sensors, and temperature from the temperature sensor alone. Both the strain and temperature coefficients can be determined experimentally by measuring their measurand-induced responses. Fig. 4.6 shows the strain and temperature responses of an AMCFBG. Based on the slopes of the linear regression fits, the strain and temperature sensitivity coefficients were 1.20 pm/με and 10.06 pm/°C, respectively. The temperature measurement was carried out when the sensor was free and unstrained. However, when it was used to measure the Al-alloy plate, due to the thermal expansion mismatch between the plate and the silica fibre, temperature response needed to be re-measured with the sensor adhered onto the plate. The measured temperature coefficient is found to be 38.12 pm/°C. Now, the strain and temperature can be expressed numerically as,

$$\Delta\varepsilon = 0.8295 \cdot \left(\Delta\lambda_{B1} - \Delta\lambda_{B2}\right); \text{ and } \Delta T = 0.0262 \cdot \Delta\lambda_{B2}, \tag{4.4}$$

where the Bragg wavelength shift, strain and temperature change are in units of pm, με and °C, respectively. To practically measure the strain and temperature change of the Al-alloy plate, one of the AMCFBG sensors was adhered firmly onto the plate with epoxy resin, whereas the other sensor was loosely attached such that it was free and unstrained from any strain field of the plate. The plate was placed inside a polyurethane foam box to minimise environmental perturbations. With the setup of Fig. 4.2, experiment was performed for a period of 18 h. By using Eq. (4.4), the strain and temperature changes are shown in Fig. 4.7. From the figure, both the strain and temperature curves changed in a much correlated manner, indicating that the strain was mainly thermally-induced. This is obvious as there was no external strain applied throughout the experiment, and unlike the previous results in Fig. 3.7, the experiment was isolated and so the thermal strain followed well with temperature change. The net change in strain and temperature during this 18 h period were about 40 με and 1.5 °C, respectively. Since the plate was placed inside a foam box that had a relatively high heat capacity, the change in temperature was a bit small. By plotting a graph of temperature vs. strain, the slope of the linear regression fit gives a thermal strain sensitivity of 33 με/°C.

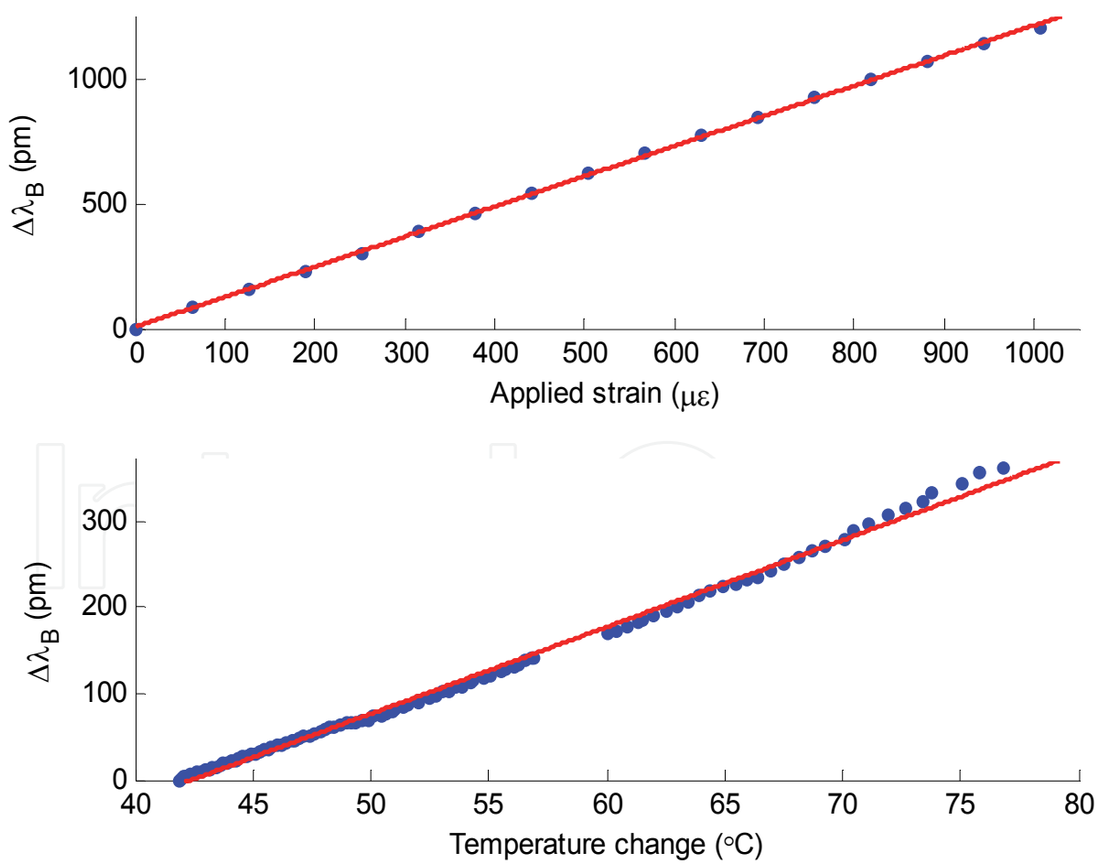

Fig. 4.6. Strain and temperature responses of the AMCFBG.

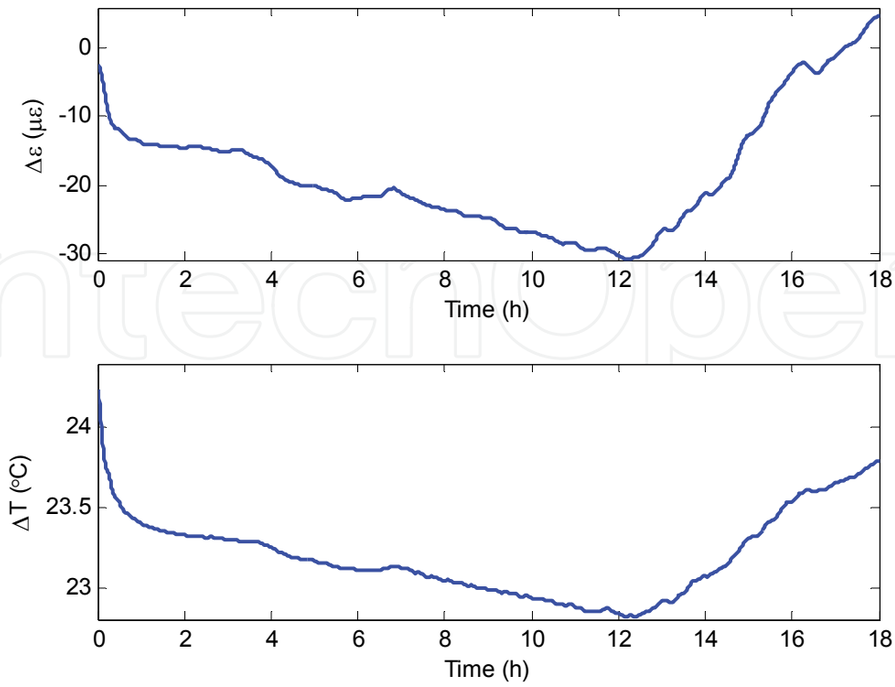

Fig. 4.7. Simultaneous measurement of strain and temperature of an Al-alloy.

5. Application case 3 – multiplexing of photonic crystal fibre sensors

In the third example, DWT was applied to the multiplexing and demultiplexing of a relatively new class of fibre – photonic crystal fibres (PCFs) (Fu et al., 2009). PCFs distinguish themselves from conventional fibers that they consist of microstructured air holes along the fibre, and a wide variety of cross-section air hole arrangements can be designed to suit different applications. The particular type of PCF used in the example was called polarisation-maintaining PCFs (PM-PCFs) that have the characteristics of high birefringence and low temperature sensitivity, and so is suitable for single parameter sensing where cross-sensitivity issue can be minimised. However, at present, all reported PCF sensors were operated as single sensors, and a main reason was due to the difficulty in demultiplexing and demodulating the multiplexed PCF sensor signals, even though the multiplexing schemes are simple and easy to implement. To overcome this, we demonstrate the use of DWT to separate the multiplexed sensor signal, such that the change from each individual sensor can be extracted and measured.

In our experimental setup, two PM-PCF sensors, PM-PCF1 and PM-PCF2, were multiplexed in series, as shown in Fig. 5.1. Each sensor unit was arranged in Sagnac interferoemter configuration with a section of PM-PCF as the birefrigent element, and the output signal can be represented by the transmission matrix as, $T = [1 - \cos(\delta)]/2$. The phase difference δ introduced by the PM-PCF with a length of L to the two light beams is wavelength dependent and is given by $\delta = 2\pi BL/\lambda$. The period of the output spectrum, i.e., the spacing between two adjacent minima, is $S=\lambda^2/(BL)$, where B is the birefringence of the PM-PCF. The birefringence change due to environmental parameters can then be detected by

measuring the 'phase shift' of minima. The output transmission spectrum of K sensor units multiplexed in series is given by (Fu et al., 2009),

$$\frac{P_{output}}{P_{input}} = 10Log_{10}\prod_{k=1}^{K}\left(\frac{1}{2}L_k\left[1-\cos(\frac{2\pi}{S_k}\lambda+\theta_k)\right]\right)[\mathrm{dB}], \tag{5.1}$$

where L_k, S_k, θ_k are the loss, the period of the output spectrum and the initial phase of the k-th sensor, respectively. Note that the output spectrum is indeed the multiplication of individual sensor signals. PM-PCF1 (length of 20 cm) was placed freely on a table, while PM-PCF2 (length of 60 cm) was placed inside a sealed pressure chamber. Pressure was

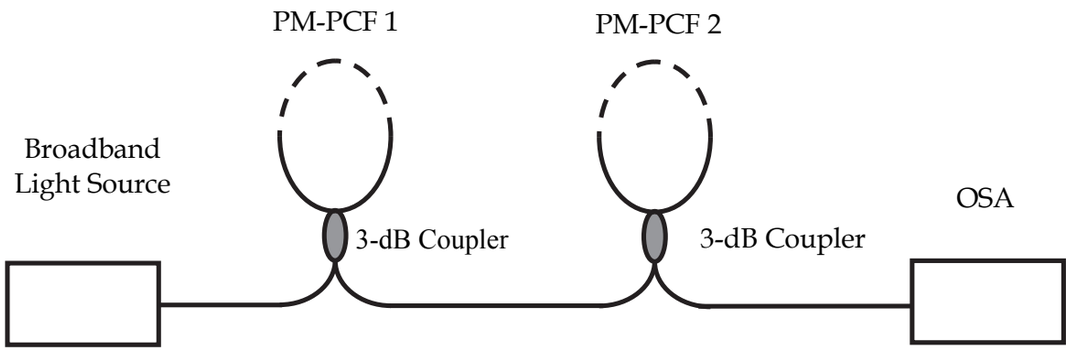

Fig. 5.1. Experimental setup of in series multiplexing technique for PM-PCF based Sagnac interferometric sensor.

applied to PM-PCF2 from 0 – 3 bars in steps of 0.5 bar, and was measured by a pressure gauge (COMARK C9557). Fig. 5.2 shows the output spectra of various pressure values measured by the OSA. In principle, to obtain the sensing information, the wavelength shift

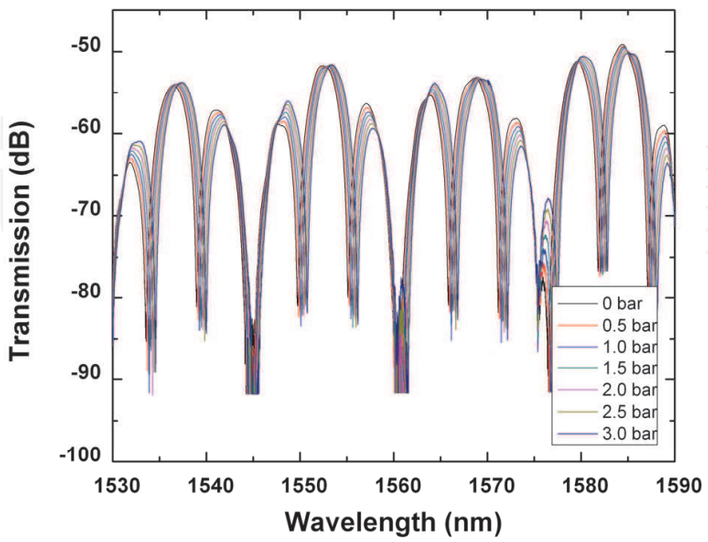

Fig. 5.2. Output transmission spectra of the two multiplexed Sagnac interferometric sensors in series with one sensor under applied pressure variations.

of the transmission minima of each sensor needs to be determined. However, as can be seen, the multiplexed sensor signal is more complex, and so simple tracing of the initial phase may not yield accurate results. We applied the DWT to the sensor signal, and the detail coefficients at two different levels are shown in Fig. 5.3. These two sets of coefficients are indeed the original sensor signal of the two sensors, and from the figure, the spectrum of PM-PCF2 shifted linearly with increasing pressure, while PM-PCF1 remained unchanged (at least the initial phase). Figs. 5.4(a) and 5.4(b) show the spectral shift of the two sensors as a function of applied pressure, and the crosstalk (includes other sources of errors, such as measurement error and ambient noise) between them, respectively. Thus, this example clearly demonstrated the capability of DWT in demultiplexing and demodulating multiplexed PCF sensor signals.

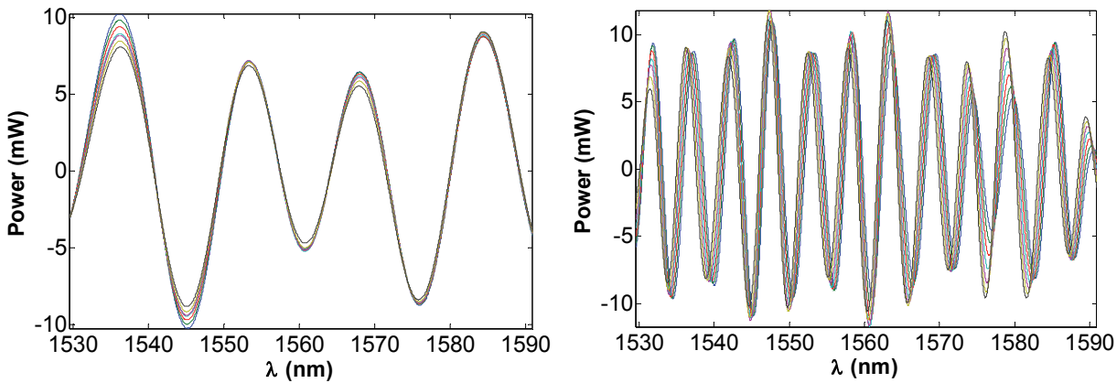

(a) (b)

Fig. 5.3. Detail coefficients of two PM-PCF sensors at two wavelet levels.

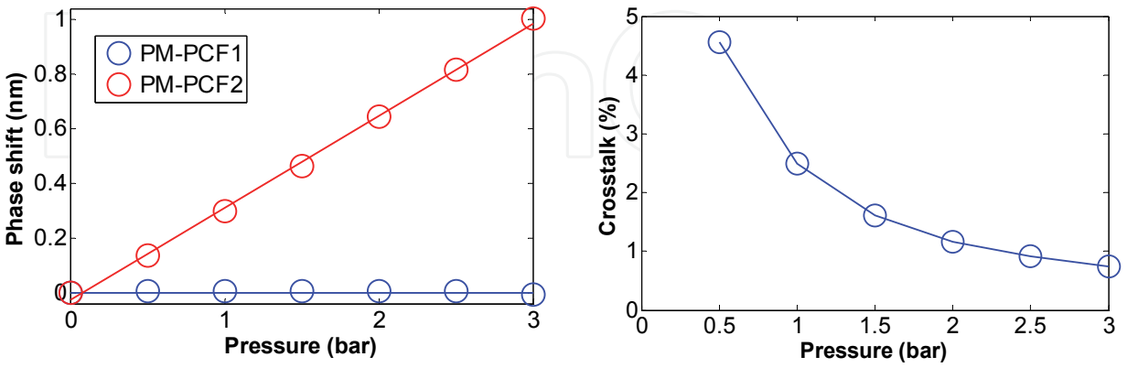

(a) (b)

Fig. 5.4. (a) Spectral phase shift and (b) crosstalk of the two PM-PCF sensor as a function of applied pressure.

6. Application case 4 – measurands analysis of novel fibre sensors

In the fourth example, DWT is used as a signal analysis tool to demodulate, analyse and interpret acquired signals from two novel fibre sensors, namely tilted moiré FBG and tilted Bragg reflector fibre laser (TBR-FL). These two sensors were proposed to perform simultaneous two-parameter sensing using only single sensing elements. The advantages are: (i) the capability of detecting more measurands using fewer sensors; (ii) the ability of mitigating the issue of cross-sensitivity (mostly temperature-induced) inherited from the sensor property (Rao, 1997); and (iii) sensor structure can be made more compact, which simplifies and eases the packaging and installation works for practical applications. It is known that, in order to measure two parameters simultaneously, either two distinctive sensor types or sensors of two different spectral characteristics are needed. The proposed sensors are unique in the sense that they are designed in such a way that, within a single sensor structure, their spectral characteristics response differently to different measurands, and so permitting them to distinguish individual measurand-induced changes. As a result, their spectral profiles are relatively more complex, and can be considered as having two parts from two different sensor types. Therefore, the spectra cannot be easily separated and analysed. However, with DWT, such complex sensor signals are readily separated without losing measurands information.

6.1 Tilted moiré fibre Bragg gratings

The tilted moiré FBG was originally proposed as a bandwidth controllable filter for telecommunications applications (Wong et al., 2010b). Here, we extended its application to fibre sensing, in particular, it was proposed as a single sensor for simultaneous two-parameter sensing (Wong et al., 2010c). The design criteria and fabrication procedure are detailed in (Wong et al., 2010c), and a typical spectrum is shown in Fig. 6.1. It can be seen that the sensor signal consists of two separate parts associated with the phase-shifted main Bragg mode (with a narrow resonance dip) and discrete cladding modes (including the ghost mode). The former is mostly confined in the core of the fibre, while the latter exist in the cladding region of the fibre. In that region, light is only loosely confined and its intensity decays exponentially along the radial direction and eventually radiates out of the fibre. As such, the cladding modes are capable of interacting with the surrounding environment at the fibre boundary, and sensing can be carried out via the principle of evanscent wave sensing.

To demonstrate the use of a single sensor for simultaneous two-parameter sensing, we performed simultaneous measurement of temperature and refractive index (RI) of an aqueous solution. The aim was to obtain the measurand-induced sensitivity coefficients independently, such that the wavelength shifts from each measurand can be unambigously determined. Thus, we carried out the characterisation experiments separately to obtain the temperature and RI sensitivity coefficients. First, temperature was varied by putting the sensor into a container filled with hot water, and the value was measured by a digital thermometer (Fluke 52II with K-type thermocouple) in the range of 43°C – 77°C, captured at every 1°C intervals. Next, the sensor was placed in a container filled with pre-mixed and saturated glucose solution (Dextrosol D-Glucose powder), and RI was varied by adding water to dilute the solution. A digital refractometer (Reichert

AR200) was used to obtain the absolute RI and temperature of the samples. The measured RI range was between 1.3331 and 1.4117, set by the RI of water and that of saturated glucose solution. The temperature (obtained from the refractormer) varied between 21.0°C – 21.6°C during the experiment. In both cases, wavelengths of the Bragg and cladding modes shifted according to measurands changes. More specifically, temperature changed the Bragg wavelength via thermo-optic effect (thermal expansion of glass fibre is very small that can be neglected), whereas the RI changed both the wavelength and transmission loss of the cladding modes. Thus, by applying the DWT, these two types of modes can be separated and their changes due to the two measurands can be extracted and analysed. Fig. 6.2 shows the detail wavelet coefficients for the (a) Bragg mode and (b) cladding modes at the 7th- and 6th-levels, respectively. Since the detail coefficients are mean removed, and so in the Bragg mode, the narrow resonance dip becomes a sharp peak, and temperature change can be measured by tracking this peak shift. As for the cladding modes, it is known that each individual cladding mode responds differently to the same measurand (e.g., RI) change, and taking an average of a number of cladding modes shifts will give more accurate readings than tracking just one particular mode. RI is thus measured by the averaged wavelength shift of about 10 cladding modes.

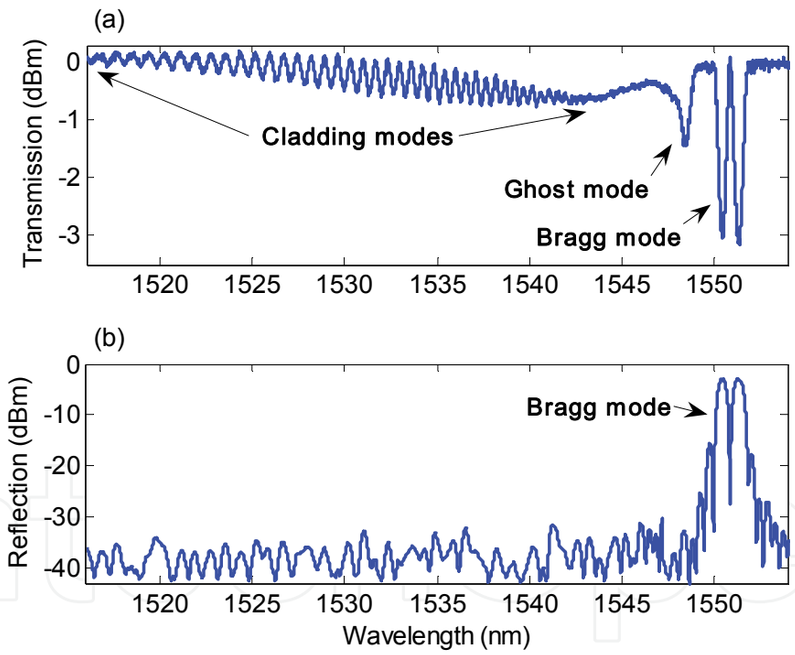

Fig. 6.1. (a) Transmission and (b) reflection spectra of the TMFBG sensor for simultaneous two-parameter sensing.

After taking the DWT to the measured spectra, Fig. 6.3 (a) shows the wavelength shifts of the wavelet coefficients for the Bragg and averaged cladding modes, respectively, as a function of temperature. The solid lines are the linear regression fits of the data points. It is clear that, in response to temperature change, the averaged cladding modes shifted by almost the same amount and in the same direction as the Bragg mode. From the regression lines, the temperature-induced sensitivity of the Bragg and averaged cladding modes are

10.53 pm/°C (with R^2 = 0.9979) and 10.48 pm/°C (with R^2 = 0.9925), respectively, which correlated very well with each other. Thus, it is sufficient to measure the temperature-only change by tracking the wavelength shift of the Bragg mode. Similarly, Fig. 6.3 (b) shows the wavelength shifts of the wavelet coefficients for the Bragg and averaged cladding modes, respectively, as a function of RI. From the figure, the Bragg mode remained unperturbed (within measurement errors), indicated that it is insensitive to RI change. The cladding modes, however, varied nonlinearly, with the curve best fitted by a polynomial function given empirically by,

$$P_{DWT}(n) = 169.58n^4 - 655.26n^3 + 843.59n^2 - 361.85n \tag{6.1}$$

(with R^2 = 0.9987) for the specified range $1.3331 \le n \le 1.4117$. Thus, for RI-only change, Eq. (6.1) can serve as a lookup table, such that by tracking the wavelength shift of the averaged cladding modes, the RI value can be obtained. By combining these two distinct measurands-induced responses, simultaneous measurement of temperature and RI is realised. Temperature change can be directly obtained from the wavelength shift of the Bragg mode, and the RI from the differential wavelength shifts between the Bragg and averaged cladding modes, i.e., the residual amount after subtracting the average shifted amount of the cladding modes from that of the Bragg mode. Fig. 6.3 (b) (and Eq. (6.1)) can then be used to find the RI value by looking-up the corresponding measured differential shift.

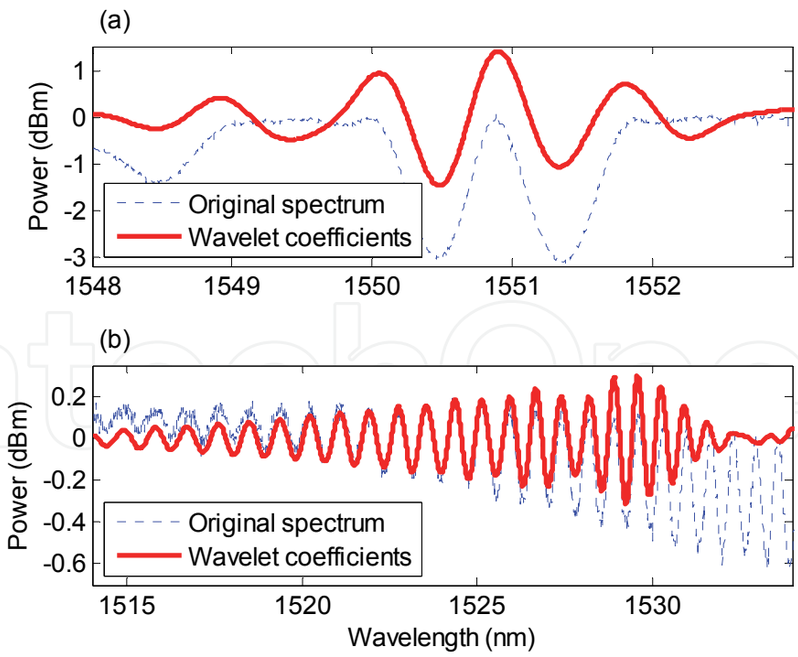

Fig. 6.2. Wavelet coefficients (solid lines) of a measured transmission spectrum: (a) 7th-level coefficients for the Bragg mode, and (b) 6th-level coefficients for cladding modes. Dotted lines are the original spectra.

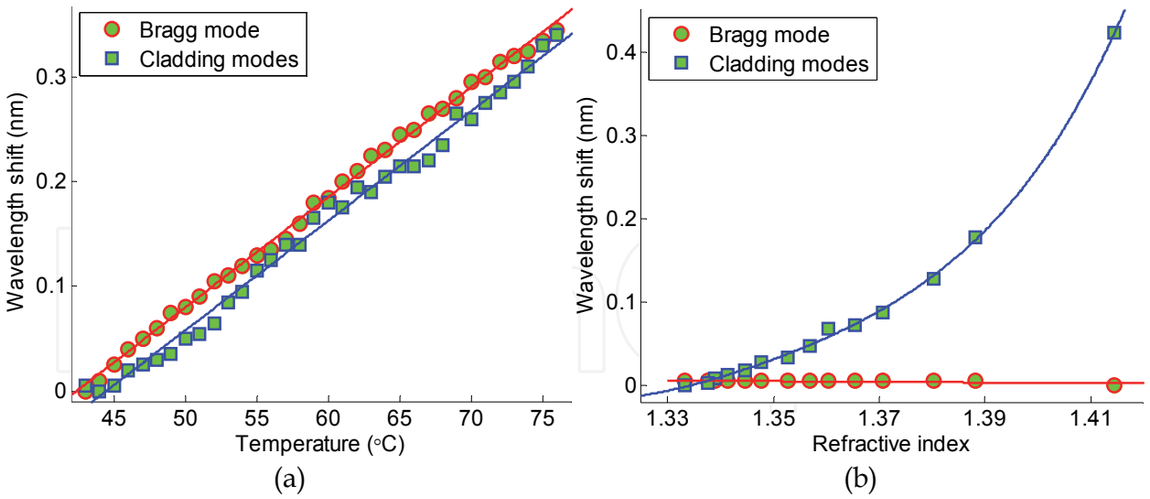

Fig. 6.3. Wavelength shifts of the wavelet coefficients for the Bragg mode and averaged cladding modes as a function of (a) temperature and (b) refractive index. Lines are the regression fits.

6.2 Tilted Bragg reflector fibre lasers

Up to present, there are mainly two types of grating-based FLs, namely distributed feedback and distributed Bragg reflector FLs. When applied in sensing, FLs have the advantage of high sensitivity, sensing output power and extinction ratio, and narrow linewidth/bandwidth. For simultaneous two-parameter sensing using single sensors, thus far, most of the proposed works are of passive type and only very few on using active sensors, e.g., fiber Raman lasers (Han et al., 2005, Tran et al., 2005) and distributed feedback FLs (Hadeler et al., 1999, 2001). TBR-FL is a new type of FL formed by a pair of wavelength and tilt-angle matched tilted FBGs (TFBGs) (Wong et al., 2011). In addition to the lasing peak, it possessed a grating tilt-induced cladding modes spectrum, which provided an extra sensing mechanism to detect the surrounding environment. We demonstrate that, with a simple experimental setup, the use of a single TBR-FL for simultaneous sensing of temperature and RI.

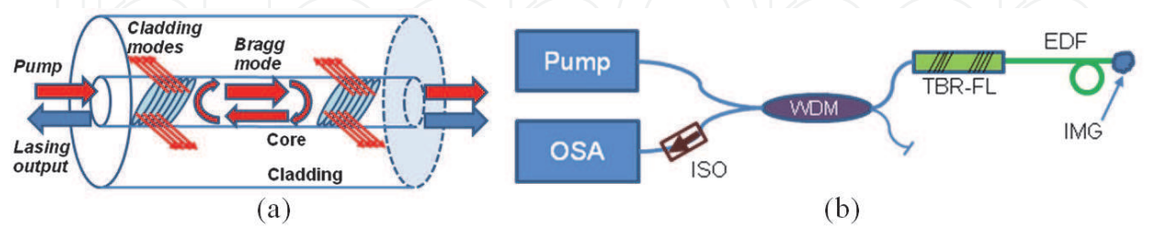

Fig. 6.4. (a) Structure of the TBR-FL, and (b) experimental setup. OSA = optical spectrum analyser, WDM = wavelength division multiplexer, EDF = erbium-doped fibre, ISO = isolator, IMG = index matching gel.

The structure of the TBR-FL comprises a pair of wavelength and tilt-angle matched TFBGs forming the resonant cavity and is depicted in Fig. 6.4 (a). The fabrication procedure is described in (Wong et al., 2011). The experimental setup depicted schematically in Fig. 6.4

(b). A laser diode was pumped to the TBR-FL via a wavelength-division-multiplexer (WDM), and the output signal was obtained by the OSA. At the other side of the FL was a continuous piece of EDF (~50 cm) looped in a diameter of ~3 cm, and so the sensor head comprised both the FL and the short coiled EDF section. Index matching gel (IMG) was applied to the far end of the EDF to minimise any reflections that may cause resonant feedback. This EDF section acted as an ASE source when excited by the excessive pump source. As such, the transmission spectrum of the constituent TFBG pair can be observed. With this setup, both the laser output and cladding modes spectra can be obtained simultaneously. A typical full spectrum is shown in Fig. 6.5 (a), which consisted of both the laser output [Fig. 6.5 (b)] and cladding modes [Fig. 6.5 (c)] spectra. Lasing occurred at the Bragg mode bound inside the core, whereas cladding modes were coupled out from the core and did not contribute to the laser operation. As mentioned, cladding modes can interact with the surrounding environment via evanescent wave, and therefore used to perform RI sensing. On the other hand, temperature change affected the FL as a whole and altered the entire spectrum (including lasing and cladding modes). Thus, simultaneous sensing was achieved by combining these two sensing properties, i.e., temperature was measured by tracking the lasing mode shift, and RI by the differential wavelength shift between the laser output and cladding modes. Similar to the previous case, the main objective was to empirically obtain the temperature and RI induced sensitivity coefficients. As such, characterisation experiments similar to that for tilted moiré FBGs were conducted [see also (Wong et al., 2011) for details], and the DWT was employed to demodulate and analyse the acquired sensor signals. Fig. 6.6 shows the wavelet coefficients of a typical measured spectrum. Detail coefficients are extracted for cladding modes [Fig. 6.6 (a)], as for the previous case; whereas approximation coefficients are extracted for the lasing mode [Fig. 6.6 (b)]. Since we are only interested in the lasing wavelength shift, approximation coefficients represent and resemble the original signal more accurately. After taking the DWT to the measured spectra, wavelength (i.e., wavelet coefficients) shifts of the laser output and averaged cladding modes (~20 modes) as a function of temperature are shown in Fig. 6.7 (a). Solid lines are the linear regression fits of the data. From the figure, both the laser output and averaged cladding modes yielded a very similar temperature-induced sensitivity, having values of 10.75 pm/°C (R^2 = 0.9991) and 10.88 pm/°C (R^2 = 0.9975), respectively. With such a high degree of correlation, it is sufficient to measure the temperature change by tracking the lasing wavelength shift alone. For RI, Fig. 6.7 (b) shows the wavelength shifts of the laser output and averaged cladding modes as a function of RI value. The laser output remained at the zero value (within measurement errors) and so have no direct relationship with RI. The averaged cladding modes varied nonlinearly with RI, and within the measured range the empirical relationship can be described by a polynomial function,

$$\Delta\lambda_{Cladding}(n) = 358.2n^4 - 1432.1n^3 + 1910.1n^2 - 849.9n \tag{6.2}$$

(R^2 = 0.9998). Thus, RI-only change can be obtained from the wavelength shift of the averaged cladding modes, as the laser output was not sensitive to it. Having established the temperature and RI sensitivity coefficients, simultaneous sensing of these two measurands using a single TBR-FL can be achieved. Temperature change can be obtained from the

wavelength shift of the laser output, whereas RI change from the differential wavelength shift between the averaged cladding modes and laser output. That is, the residual amount of the wavelength shift of the averaged cladding modes after subtracting from that of the laser output. As such, Fig. 6.7 (b) can be used as a look-up table to find the RI from the differential wavelength shift.

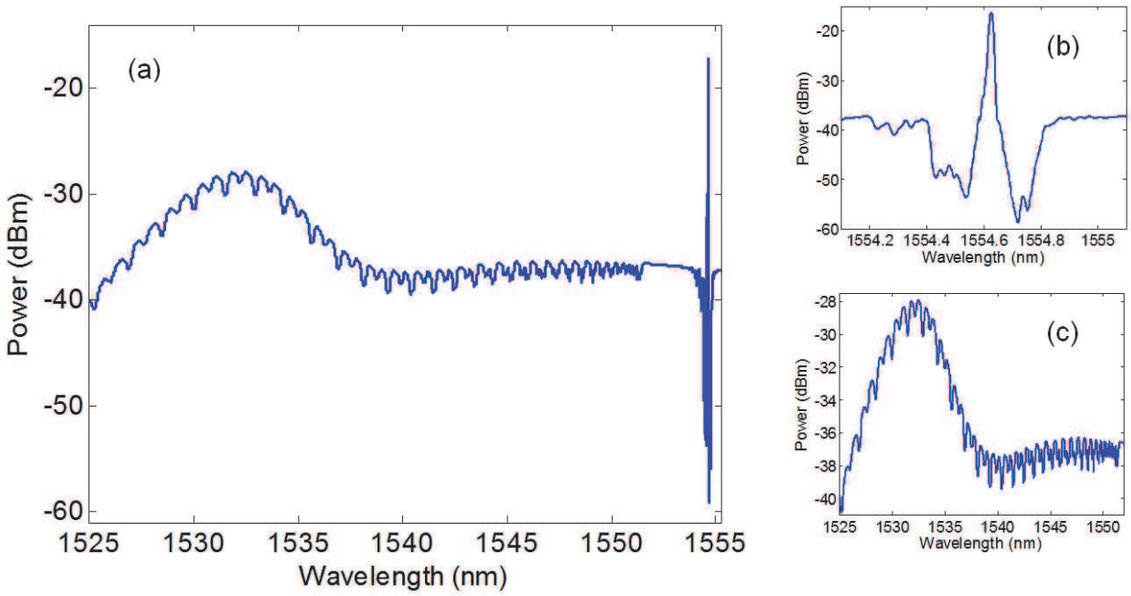

Fig. 6.5. (a) Full spectrum of the TBR-FL sensor; and the magnification around (b) the laser output and (c) cladding modes spectrum.

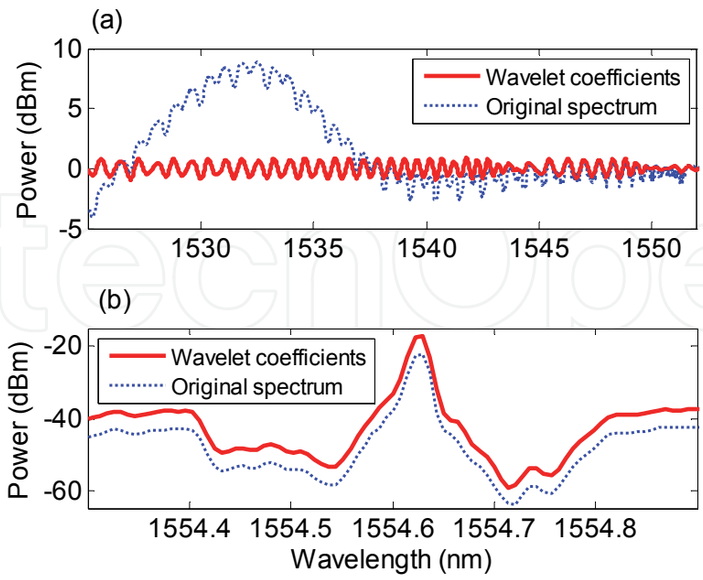

Fig. 6.6. Wavelet coefficients of a measured TBR-FL spectrum: (a) 6th-level detail coefficients for the cladding modes, and (b) 2nd-level approximation coefficients for the Bragg mode. Dotted lines are the original spectra (manually offset) for comparison.

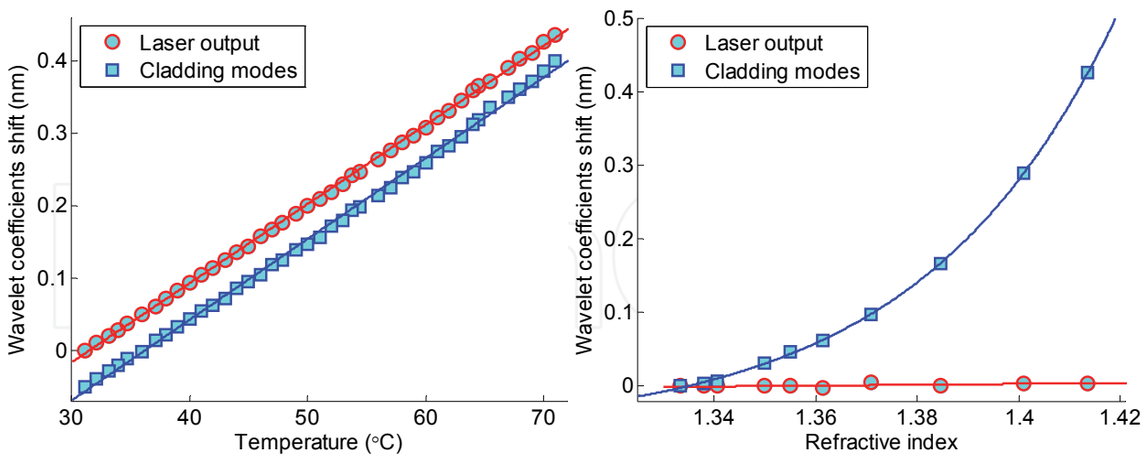

Fig. 6.7. Wavelet coefficients shift of the laser output and averaged cladding modes as a function of (a) temperature and (b) refractive index. Lines are the regression fits.

7. Conclusion

A review of the applications of DWT in optical fibre sensing is presented. Several representative application examples proposed by the authors have been discussed; and based on the implementation of DWT, novel signal processing techniques and fibre sensors have been designed and proposed. The concepts of DWT demodulation technique and the BLT wavelet denoising were introduced and applied to various application examples. First, we proposed and employed the DWT to demodulate and demultiplex a multiplexed FFI and FBG sensor system. Second, we designed a novel type of FBG (the AMCFBGs), and based on their unique overlapping properties, a new multiplexing technique called spectral overlap multiplexing was proposed and demonstrated. Third, DWT was employed in the multiplexing and demultiplexing of PCF-based sensors array, a relatively new class of fibre sensors that, up until now, has always been used as single sensors. Fourth, DWT was used as a signal analysis tool for two novel fibre sensors, namely the tilted moiré FBG (a passive sensor) and the TBR-FL (an active sensor) sensors. Complex sensor signals were separated and demodulated to obtain the individual measurands-induced changes, such that single sensing elements can perform simultaneous two-parameter sensing. In addition, BLT was applied in all the above cases to denoise sensor signals automatically during the use of the DWT demodulation technique.

8. Acknowledgment

Funding for an ARC Linkage Project (Project ID: LP0884100) from the Australian Research Council and the Roads and Traffic Authority, NSW, Australia, is gratefully acknowledged. Funding for an International Science Linkage Grant (Project ID: CG130013) from the Department of Industry, Innovation, Science and Research (DIISR), Australia, is also gratefully acknowledged.

9. References

Bang, H. J. & Kim, C. G. (2010). Study on the wavelet decomposed details of impact induced AE signals in composite laminates using fiber Bragg grating sensors, *Proc. SPIE*, Vol.7647, pp. 76473E

Chan, C. C.; Ni, N.; Sun, J.; Chu, Y. C.; Tang, Y.; Poh, C. L. (2007). Improving the detection accuracy in fiber Bragg grating sensors by using a wavelet filter, *J. Optoelectron. Adv. Mater.,* Vol.9, No.8, pp. 2376-2379

Chan, C. C.; Ni, N.; Sun, J.; Chu, Y. C.; Tang, Y.; Poh, C. L. (2010). Interferometric noise suppression in fiber Bragg grating sensors by using wavelet filter, *J. Optoelectron. Adv. Mater.,* Vol.12, No.6, pp. 1241-1246

Childs, P.; Wong, A. C. L.; Yan, B. B.; Li, M. & Peng, G. D. (2010). A review of spectrally coded multiplexing techniques for fibre grating sensor systems, *Meas. Sci. Technol.,* Vol.21, pp. 094007 (7pp)

Daubechies, I. (1992). *Ten Lectures on Wavelets,* Society for Industrial and Applied Mathematics, Philadelphia, PA, U. S. A.

Donoho, D. L. & Johnstone, I. M. (1994) Ideal spatial adaption by wavelet shrinkage *Biometrika,* Vol.81, pp. 425–55

Fu, H. Y.; Wong, A. C. L.; Childs, P. A.; Tam, H. Y.; Liao, Y. B.; Lu, C. & Wai, P. K. A. (2009). Multiplexing of polarization-maintaining photonic crystal fiber based Sagnac interferometric sensors, *Opt. Express,* Vol.17, pp. 18501-18512

Gangopadhyay, T. K.; Chakravorti, S.; Bhattacharya, K. & Chatterjee, S. (2005). Wavelet analysis of optical signal extracted from a non-contact fibre-optic vibration sensor using an extrinsic Fabry–Perot interferometer, *Meas. Sci. Technol.*, Vol.16, pp. 1075–1082

Gangopadhyay, T.K.; Chakravorti, S.; Chatterjee, S. & Bhattacharya, K. (2006). Time-frequency analysis of multiple fringe and nonsinusoidal signals obtained from a fiber-optic vibration sensor using an extrinsic Fabry-Perot interferometer, *J. Lightw. Technol.,* Vol.24, No.5, pp. 2122-2131

Hadeler, O.; Rønnekleiv, E.; Ibsen, M. & Laming, R. I. (1999). Polarimetric distributed feedback fiber laser sensor for simultaneous strain and temperature measurements, *Appl. Opt.*, Vol.38, pp. 1953–1958

Hadeler, O.; Ibsen, M. & Zervas, M. N. (2001). Distributed-feedback fiber laser sensor for simultaneous strain and temperature measurements operating in the radio-frequency domain, *Appl. Opt.*, Vol.40, pp. 3169–3175

Han, Y. G.; Tran, T. V. A.; Kim, S. H. & Lee, S. B. (2005). Multiwavelength Raman-fiber-laser-based long distance remote sensor for simultaneous measurement of strain and temperature, *Opt. Lett.*, Vol.30, pp. 1282–1284

Jones, K. J. (2000a). Wavelet edge detection applied to be used with composite embedded fiber optic sensors, *Proc. SPIE*, Vol.3986, pp. 397-406

Jones, K. J. (2000b). Wavelet crack detection algorithm for smart structures, *Proc. SPIE*, Vol.4328, pp. 306-313

Lamela-Rivera, H.; Macia-Sanahuja, C. & Garcia-Souto, J. A. (2003). Detection and wavelet analysis of partial discharges using an optical fibre interferometric sensor for high-power transformers, *J. Opt. A-Pure Appl. Opt.,* Vol. 5, No.1, pp. 66-72

Lee, B. (2003). Review of present status of optical fiber sensors, *Opt. Fiber Technol.*, Vol.9, pp. 57-79

Mallet, S. G. (1998). *A Wavelet Tour of Signal Processing,* Academic Press, Burlington, MA, U. S. A.

Mallet, S. G. (1989). A theory for multiresolution signal decomposition: the wavelet representation, *IEEE Trans. Pattern Anal. Mach. Intell.,* Vol.11, pp. 674–693

Rao, Y. J. (1997). In-fibre Bragg grating sensors, *Meas. Sci. Technol.*, Vol.8, pp. 355-375

Sidney Burrus, C.; Gopinath, R. A.; & Guo, H. (1998). *An Introduction to Wavelets and Wavelet Transforms,* Prentice Hall, Upper Saddle River, NJ, U. S. A.

Staszewski, W. J.; Gareth Pierce, S.; Worden, K.; Philp, W. R.; Tomlinson, G. R. & Culshaw, B. (1997). Wavelet signal processing for enhanced Lamb wave defect detection in composite plates using optical fiber detection, *Opt. Eng.*, Vol.36, No.7, pp. 1877–1888

Tomic, M.; Dinovic, Z. & Petricevic, S.; (2010). Fiber-optic pressure sensor based on Fizeau receiving interferometer, *Proceedings of the 33rd International Convention MIPRO*, pp. 100-104, Opatija, Croatia, May 24-28, 2010

Tran, T. V. A.; Han, Y. G.; Kim, S. H. & Lee, S. B. (2005). Long-distance simultaneous measurement of strain and temperature based on a fiber Raman laser with a single fiber Bragg grating embedded on a quartz plate *Opt. Lett.*, Vol.30, pp. 1632–1634

Vetterli, M. & Kovacevic, J. (1995). *Wavelets and Subband Coding,* Prentice Hall, Upper Saddle River, NJ, U. S. A.

Wang, G.; Pran, K.; Sagvolden, G.; Havsgard, G. B.; A E Jensen, A. E.; Johnson, G. A. & Vohra, S. T. (2001). Ship hull structure monitoring using fibre optic sensors, *Smart Mater. Struct.,* Vol.10, pp. 472-478

Wong, A. C. L.; Phillips, C. J. E. & Peng, G. D. (2005). Improved demodulation algorithm for spatial-frequency multiplexed fibre-optic Fizeau strain sensor system, Proceedings of 30th Australian Conference on Optical Fibre Technology, Sydney, Australia

Wong, A. C. L.; Childs, P. A. & Peng, G. D. (2006a). Simultaneous demodulation technique for a multiplexed fibre Fizeau interferometer and fibre Bragg grating sensor system, *Opt. Lett.*, Vol.31, pp. 23-25

Wong, A. C. L.; Childs, P. A. & Peng, G. D. (2006b). Multiplexed fibre Fizeau interferometer and fibre Bragg grating sensor system for simultaneous measurement of quasi-static strain and temperature using discrete wavelet transform, *Meas. Sci. Technol.,* Vol.17, pp. 384-392

Wong, A. C. L.; Childs, P. A. & Peng, G. D. (2007a). Multiplexing technique using amplitude-modulated chirped fibre Bragg gratings, *Opt. Lett.*, Vol.32, pp. 1887-1889

Wong, A. C. L.; Childs, P. A. & Peng, G. D. (2007b). Spectrally-overlapped chirped fibre Bragg grating sensor system for simultaneous two-parameter sensing, *Meas. Sci. Technol.,* Vol.18, pp. 3825-3832

Wong, A. C. L.; Childs, P. A. & Peng, G. D. (2010a). Spectrally coded multiplexing techniques in fibre-optic sensor systems, In: *Trends in Photonics*, J. Canning (ed.), Chapter 8, pp. 233-276, Transworld Research Network, ISBN: 978-81-7895-441-7, Kerala, India

Wong, A. C. L.; Giovinazzo, M.; Tam, H. Y.; Lu, C. & Peng, G. D. (2010b). Tilted moiré fiber Bragg grating optical filters with controllable passband and stopband, *J. Lightw. Technol.*, Vol.18, pp. 898-904

Wong, A. C. L.; Giovinazzo, M.; Tam, H. Y.; Lu, C. & Peng, G. D. (2010c). Simultaneous two-parameter sensing using a single tilted moiré fiber Bragg grating with discrete wavelet transform technique, *IEEE Photon. Technol. Lett.,* Vol.22, pp. 1574-1576

Wong, A. C. L.; Chung, W. H.; Lu, C. & Tam, H. Y. (2011). Single tilted Bragg reflector fiber laser for simultaneous sensing of refractive index and temperature, *Opt. Express,* Vol.19, pp. 409-414

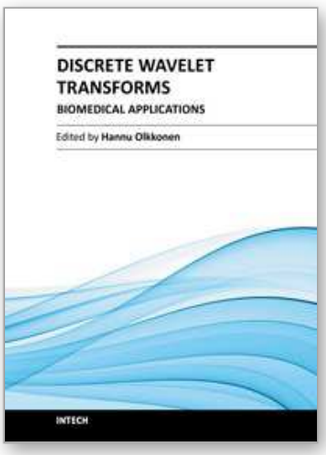

Discrete Wavelet Transforms - Biomedical Applications

Edited by Prof. Hannu Olkkonen

ISBN 978-953-307-654-6
Hard cover, 366 pages
Publisher InTech
Published online 12, September, 2011
Published in print edition September, 2011

The discrete wavelet transform (DWT) algorithms have a firm position in processing of signals in several areas of research and industry. As DWT provides both octave-scale frequency and spatial timing of the analyzed signal, it is constantly used to solve and treat more and more advanced problems. The present book: Discrete Wavelet Transforms - Biomedical Applications reviews the recent progress in discrete wavelet transform algorithms and applications. The book reviews the recent progress in DWT algorithms for biomedical applications. The book covers a wide range of architectures (e.g. lifting, shift invariance, multi-scale analysis) for constructing DWTs. The book chapters are organized into four major parts. Part I describes the progress in implementations of the DWT algorithms in biomedical signal analysis. Applications include compression and filtering of biomedical signals, DWT based selection of salient EEG frequency band, shift invariant DWTs for multiscale analysis and DWT assisted heart sound analysis. Part II addresses speech analysis, modeling and understanding of speech and speaker recognition. Part III focuses biosensor applications such as calibration of enzymatic sensors, multiscale analysis of wireless capsule endoscopy recordings, DWT assisted electronic nose analysis and optical fibre sensor analyses. Finally, Part IV describes DWT algorithms for tools in identification and diagnostics: identification based on hand geometry, identification of species groupings, object detection and tracking, DWT signatures and diagnostics for assessment of ICU agitation-sedation controllers and DWT based diagnostics of power transformers.The chapters of the present book consist of both tutorial and highly advanced material. Therefore, the book is intended to be a reference text for graduate students and researchers to obtain state-of-the-art knowledge on specific applications.

How to reference

In order to correctly reference this scholarly work, feel free to copy and paste the following:

Allan C. L. Wong and Gang-Ding Peng (2011). Applications of Discrete Wavelet Transform in Optical Fibre Sensing, Discrete Wavelet Transforms - Biomedical Applications, Prof. Hannu Olkkonen (Ed.), ISBN: 978-953-307-654-6, InTech, Available from: http://www.intechopen.com/books/discrete-wavelet-transforms-biomedical-applications/applications-of-discrete-wavelet-transform-in-optical-fibre-sensing

INTECH
open science | open minds

InTech Europe
University Campus STeP Ri
Slavka Krautzeka 83/A

InTech China
Unit 405, Office Block, Hotel Equatorial Shanghai
No.65, Yan An Road (West), Shanghai, 200040, China

www.intechopen.com

51000 Rijeka, Croatia
Phone: +385 (51) 770 447
Fax: +385 (51) 686 166
www.intechopen.com

中国上海市延安西路65号上海国际贵都大饭店办公楼405单元
Phone: +86-21-62489820
Fax: +86-21-62489821

IntechOpen

IntechOpen